Materials Today Communications 37 (2023) 107043

Contents lists available at ScienceDirect

Materials Today Communications

journal homepage: www.elsevier.com/locate/mtcomm

Influence of thermoelastic boundary conditions on the mechanical strength of cold-rolled silicon steels

Caio Moura [a], Andres F. Galvis [b,*], Paulo Sollero [a]

[a] School of Mechanical Engineering, University of Campinas, Campinas 13083-860, SP, Brazil
[b] School of Mechanical and Design Engineering, University of Portsmouth, Portsmouth PO1 3DJ, UK

ARTICLE INFO

Dataset link: http://dx.doi.org/10.17632/d24fmr56db.1

Keywords:
Thermoelasticity
Cold-rolled silicon steel
Crystallographic texture
Anisotropy
Boundary element method

ABSTRACT

A numerical and experimental framework is proposed for an uncoupled thermoelastic analysis of anisotropic cold-rolled steel alloys Fe-3%Si to explore the influence on the material strength when subjected to thermal and inertial loads. Following the stationary thermoelasticity formulation of the boundary element method (BEM), this model focuses on the 2D study of these materials when the elastic properties are temperature-dependent and inertial forces are considerable. Validations and an industrial application are shown to illustrate the feasibility of using the framework proposed here to study the thermomechanical behavior of the Fe-3%Si, taking into account the influence of temperature on its mechanical and thermal properties. Finally, a complete database is provided for reproducibility purposes.

1. Introduction

The constant growth in the complexity of engineering projects encourages technological advancement and the use of adequate computational tools to enable increasingly efficient and competitive outcomes. It is common for a large amount of equipment, machinery, and even structures to contain components that operate under temperature gradients that rise to thermoelastic stresses. Some applications are, e.g., internal combustion engines, electrical machines, or braking systems. Thermoelastic stresses are linked to other important engineering phenomena, including fatigue, failure, crack nucleation, and other events that jeopardize the component's structural integrity. Constitutive equations that describe the thermoelastic phenomenon can be found in the literature [1–3]. Therefore, it is crucial to comprehend these stresses, strains, and damage caused by thermal loads to apply the proper failure criterion and technical considerations for the design of components.

Microscopically, cold-rolled silicon steels have a body-centered cubic lattice structure within their grains. The crystallographic orientation of each grain is not random [4]. The constitutive model of each grain is considered an anisotropic elastic media, with elastic properties varying depending on the lattice structure and chemical composition. A set of non-periodic polycrystal aggregates represents each material point at the macroscale. Then, a non-random morphological grain assembled with its distinct crystalline orientations can be artificially modeled [5–10] to approximate the macroscopic elastic properties [11–13] of the material. In addition, the elastic constants of a single crystal and the distribution of crystal orientation and grain size, which are experimentally determined using Electron Backscatter Diffraction (EBSD), can be used to estimate Young's modulus of textured and non-textured materials [12].

In general, studies that evaluated the effects of thermal and inertial loads approximated the cold-rolled silicon steel elastic properties as isotropic [14,15]. However, silicon steels produced by the cold rolling process show orthotropic elastic properties. The parameters of the cold rolling process influence the anisotropy of the ferritic steel mechanical properties [16,17]. Usually, this steel has peaks of texture intensity at (110)[001], Goss component, and weak γ^* fiber with peaks close to (111)[112] after the recrystallization at the end of the cold rolling process [18]. Hence, the grains have preferred orientations that could promote an elastic orthotropy in the macroscale properties.

One industrial application where these steels are highly employed is in the rotors of electrical motors, as they provoke severe operational conditions. In particular, this scenario is ideal for the analysis and the purpose of this research, however, the framework presented in this work is general and can be considered in many other industrial applications. Therefore, the high rotational speeds infer considerable stresses due to inertial loads on the rotor [19,20]. Also, the effect of thermal loading added to inertial loading considering the Fe-3%Si temperature-dependent elastic properties shows that thermal effects could reduce the safety factors, increasing the possibility of damage and resonance [21,22]. Once a yield failure for rolled sheets of polycrystalline metal where the texture is fine-grained is dependent on its

* Corresponding author.
E-mail address: andres.galvis@port.ac.uk (A.F. Galvis).

https://doi.org/10.1016/j.mtcomm.2023.107043
Received 25 May 2023; Received in revised form 18 August 2023; Accepted 2 September 2023
Available online 6 September 2023

mechanical properties and stresses [23], it is important to consider its elastic, mechanical, and thermal properties as temperature-dependent. Such properties can be experimentally obtained by isothermal tensile, thermal conductivity, and thermal expansion standardized tests [24–30].

Generally, the thermal field applied in electrical rotors is generated from the joule effect and commonly obtained from electrical motors' electromagnetic and thermal analysis [31,32]. Since the temperature is prescribed in its thermoelastic analysis, all physical variables are independent of time. i.e., the material behavior can be described by the uncoupled thermoelasticity formulation [2]. The approach consists of solving first the heat conduction equation, yielding the temperature distribution on the body. The temperature and heat flux can also be prescribed. Finally, the elastic solution is obtained from the thermal expansion's generalized body force. The differential equations are solved by Boundary Element Method (BEM), which stands out with greater applicability to thermoelastic solutions among the existing numerical approaches [2,33,33–35].

This work performs an experimental cold-rolled Fe-3%Si temperature-dependent characterization, providing a material properties database. Then, an uncoupled thermoelastic analysis of anisotropic cold-rolled steels where the material is subjected to thermal and inertial loads is treated. Following the uncoupled thermoelasticity BEM formulation, the model focuses on the 2D study of these materials when the elastic properties are temperature-dependent. At the end, the stresses and displacements of an electric motor rotor are calculated under various combinations of inertial and thermal loads, allowing a discussion about the thermal loadings' influence on material failure criteria.

2. Elastic, mechanical and thermal properties

Samples of cold-rolled silicon steel with 3.3% Si (Fe-3%Si) and 0.30 thickness were commercially acquired. Then, the samples were submitted to experimental tests to determine their physical properties, which are of interest in this work. This material has a recrystallized microstructure by an annealing process, i.e., a polycrystalline structure in the ferritic phase with a body-centered cubic (BCC) system where the grain size and shape are uniformly distributed and with proper crystalline orientations and planes.

At the microscale, each grain is considered an anisotropic body regarding its elastic properties. At the macroscale, the polycrystal elastic constitutive equation is defined as anisotropic in the function of its grain size and crystallographic texture. This section takes the following experimental approach to obtain the cold-rolled silicon steel elastic tensor (Fig. 1). First, the lattice constant of the Fe-3%Si is calculated by Bragg's law using X-ray diffraction data collected. From the lattice constant and Fe-3%Si chemical composition, the single crystal temperature-dependents elastic constants are defined. These elastic constants are shown in [36]. The Electron Backscatter Diffraction (EBSD) data are given in sequence, characterizing the polycrystal aggregate regarding grain size and crystallographic orientations. From the EBSD data and temperature-dependent elastic constants of the Fe-3%Si single crystal [36], the elastic constants of the polycrystal aggregate are calculated by from Reuss and Voigt's (V-R) average homogenization models [12,37] and reduced to a plane stress case. The Fe-3%Si elastic constants obtained by V-R models are compared to experimental data acquired from the tensile test to validate the approach. In the end, the experimentally obtained mechanical properties are defined as anisotropic, and the thermal expansion and thermal conductivity coefficients are defined as isotropic.

2.1. X-ray crystallography

The crystal lattice needs to be known to define from [36] the proper single-crystal temperature-dependent elastic constants. X-ray crystallography is an experimental technique to determine a crystal's atomic and molecular structure by the diffraction caused in the incident beam by the specimen crystalline structure into specific directions [38]. To obtain the x-ray diffractometry graph of Fe-3%Si alloy, a sample with dimensions of 50×50 mm was cut and sanded with sandpaper of 120, 220, 320, 500, and 600 grit designation. Then, the sample was washed with water and mild soap. Subsequently, a chemical polishing with a solution of HNO_3 (12%) and HF (3%) at an approximate temperature of 55 °C was carried out to remove residual deformations. A diffractometer X'Pert Philips® collected the crystal diffractions data, equipped with a high precision goniometer and ATC-3 Prefix® texture cradle and anode material made of Cu ($\lambda = 1.5406$ Å), where λ is the lattice constant. The crystal structure's Miller indices and Bragg's angle 2Θ were then obtained from the diffraction graph plotted from the data collected. Finally, the crystal lattice was calculated by Bragg's law Eq. [38].

Fig. 2 shows the X-ray diffraction graph of the Fe-3%Si sample with 7650 kg/m^3 of density at 25 °C. The intensity peaks given in counts per second show the diffraction angles observed in the sample. The attained peaks at different 2Θ values occurred close to the standard cited by International Centre for Diffraction Data Sample (JCPDS) card number 65-4899 for Fe-α [39].

From Bragg's angle Θ, the Fe-3%Si lattice constant a was calculated. Results are shown in Table 1, comparing the lattice constant for Fe-α and Fe-3%Si, it is possible to observe that the substitutional Si atoms caused a low distortion in the crystal lattice, reducing the value of the constant lattice from 2.8608 Åto 2.8601 Å. Although small, the lattice structure distortion is due to the difference in atomic radius between the Si (1.46 Å) and Fe (1.72 Å) atoms.

Table 1
Fe-3%Si and Fe-α lattice constants.

Fe-3%Si [Å]	Fe-α [Å]
2.8601	2.8608

2.2. Electron backscattered diffraction

The Electron Backscatter Diffraction (EBSD) technique was used to measure grain sizes and their respective crystallographic directions. The EBSD is a scanning electron microscope (SEM) based technique that provides crystallographic data regarding a specimen microstructure [40]. To perform the analysis, six samples of Fe-3%Si alloy were cut in different regions on the steel sheet. Then, the samples were embedded in a resin, sanded with sandpaper of 120, 220, 320, 500, and 600 grit designation, and mechanically polished with the diamond polishing agent on 9 μm, 3 μm, and 1 μm. Subsequently, the samples were polished in a solution containing 10 mL of DP-Lubricant Blue and 40 mL of 0.05 μm colloidal silica for 60 min in the polisher.

The analyses were performed in a SEM Philips XL-30 FEG® with $LabB_6$ filament, equipped with the TSL EBSD system. The step used in the analysis was 3 μm. The samples were collected in different regions of a silicon steel plate. The data obtained from the EBSD analyses were post-processed using the EDAX OIM Analysis™ software. Points on maps with a confidence index (CI) below 0.095 were disregarded in the data analysis. The map of crystallographic orientations was then plotted for each point collected in an Inverse Pole Figure (IPF) map, and the grain size, with its associated crystallographic orientation, was obtained.

Fig. 3 shows the IPF of six different fields collected by the EBSD technique in a scanning electron microscope in a Fe-3%Si sample. Altogether 536 800 points were indexed, resulting in 2290 grains collected with an average diameter of 44 μm with their respective associated crystallographic directions. It is observed that the microstructure is in a recrystallized state with equiaxed grains.

Table 2 shows a portion of the collected data for each grain. In the data set, the crystallographic directions are given in Euler angles, which can be transformed into Miller indices to describe the crystal

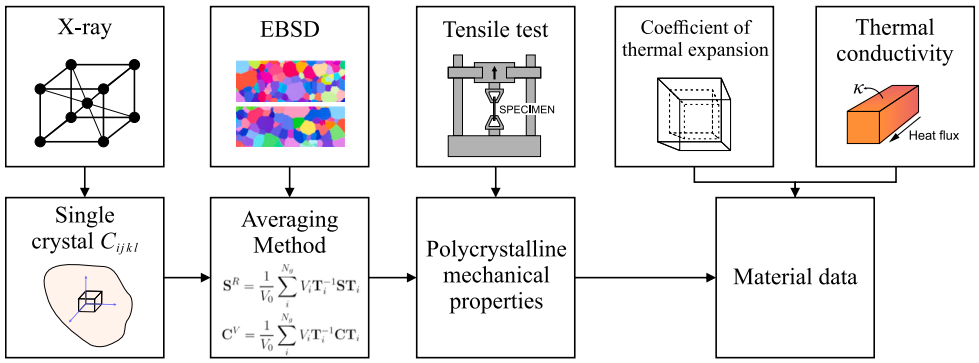

Fig. 1. Experimental approach.

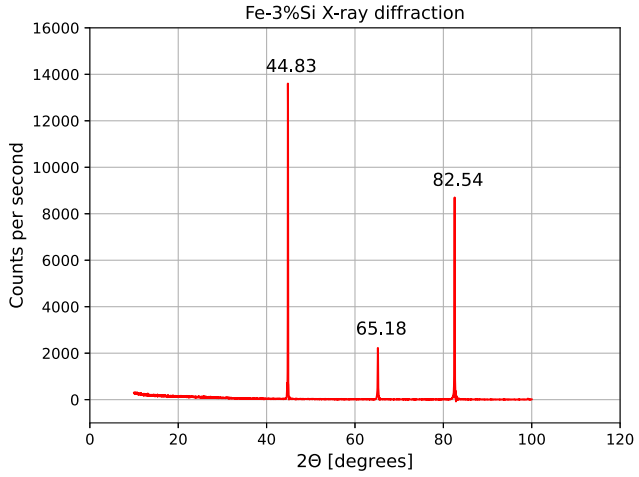

Fig. 2. Fe-3%Si X-ray diffraction.

Table 2
Fe-3%Si samples EBSD data.

Grain	Φ_1 [rad]	Φ [rad]	Φ_2 [rad]	Area [μm^2]	Diameter [μm]
1	2.85594	0.24988	3.24554	9.900e+001	11.23
2	5.71068	0.87976	0.77531	6.480e+002	28.72
3	0.09743	0.60250	0.27292	1.386e+003	42.01
⋮	⋮	⋮	⋮	⋮	⋮
2290	3.30461	0.46553	2.22333	5.940e+002	27.50

directions (Fig. 3) or directly used to define the rotation matrices in the Eqs. (4) and (6) to obtain the stiffness tensor $\mathbf{C}^{V-R}$ of overall polycrystal aggregate.

Fig. 4 shows the volumetric fraction of each grain size present in the samples. The grain size is considered in Eqs. (4) and (6) as an averaging term, defining the weight of each grain in the $\mathbf{C}^{V-R}$ calculation.

2.3. Tensile properties

The tensile test describes how the material will mechanically react to forces applied in traction. In this work, the following material constants are obtained from the stress–strain curve: Young's modulus (E_i), shear modulus (G), Poisson's ratio (η), 0.2% offset yield strength (σ_y), ultimate tensile strength (σ_{uts}), uniform elongation (A_g), elongation at break (A_{80}), and Lankford coefficient (r_{x_i}). The experimental analysis was done in triplicate tests in each principal direction x_i, longitudinal (x_1), and transversal (x_2) direction concerning the cold-rolled direction. Isothermal tensile tests were conducted at room temperature (25 °C) and 150 °C.

For room temperature (25 °C), the specimens were prepared according to ASTM E8/E8M standard [41] in sheet-samples types with 12.5 mm wide. The specimens were prepared by the CNC milling process. The traction test was carried out using a traction test machine INSTRON 5583® where the specimens were subjected to a strain rate of 1.7×10^{-1} s^{-1}. An INSTRON 2663-821 video extensometer connected to a video main board operating at 500 Hz measures the sample displacement, and a 150 kN load cell measures the loading.

For the specimen at 150 °C, the isothermal tensile test was conducted according to ISO 6892-2 standard [24] with a type 2 specimen according to Table B.1. in a strain rate of 2.5×10^{-4} s^{-1}. The specimens were prepared by the CNC milling process. The traction test was carried out using a traction test machine EMIC. A three-zone split furnace was used to heat the sample. The test is isothermal, and contact thermocouples measure the sample temperature. The furnace structure around the sample prevents the measurement of the sample displacements by the video extensometer. Due to this, displacements are measured by the gripping device displacement. It is not possible to accurately measure the modulus of elasticity and Lankford coefficient at 150 °C since the gripping device and other equipment parts' elastic displacements are included in the tensile curve.

Fig. 5 shows the tensile curves at 25 °C and 150 °C in x_i directions, separating each tensile curve with its proper sample identification, informing the temperature load to which each one was submitted.

The mechanical properties described here were obtained for 25 °C and 150 °C tensile curves. However, as mentioned earlier, it is not possible to obtain the specimen elastic modulus from the isothermal tensile curve at 150 °C. The results are shown in Table 3, where all values shown in the Table are averaged from triplicate samples.

It is observed that the elongation increased with the increment of the temperature. At the same time, the yield and ultimate tensile strengths decreased, i.e., it is observed an increase in the material ductility whilst the temperature increased, as expected in metallic materials [25,26]. For direction x_1, σ_y and σ_{uts} were reduced in 24.20% and 8.89%, respectively, when the specimen was heated from 25 to 150 °C. For direction x_2, σ_y and σ_{uts} were reduced in 25.02% and 4.99%, respectively, when the specimen was heated from 25 to 150 °C.

A linear relationship is assumed between yield strength and temperature increment for ferritic steels (BCC) in temperatures below 400 °C [42,43]. Then, in this work, the yield strength is directly related to the temperature by a linear equation. Therefore, based on Table 3, the Fe-3%Si yield strength in MPa units along the x_1 direction as a function of temperature T in °C is defined by the equation

$$\sigma_{x_1}(x_1, T) = -0.8328\,T + 450.92, \tag{1}$$

and, for x_2 direction

$$\sigma_{x_2}(x_2, T) = -0.892\,T + 467.80. \tag{2}$$

2.4. Elastic constitutive model

Each grain is modeled as a linear elastic anisotropic continuum body for an aggregate of several grains. The constitutive relation of stress–strain fields is given by a stiffness tensor $\mathbf{C} \equiv C_{ijkl}$, and its anisotropy is

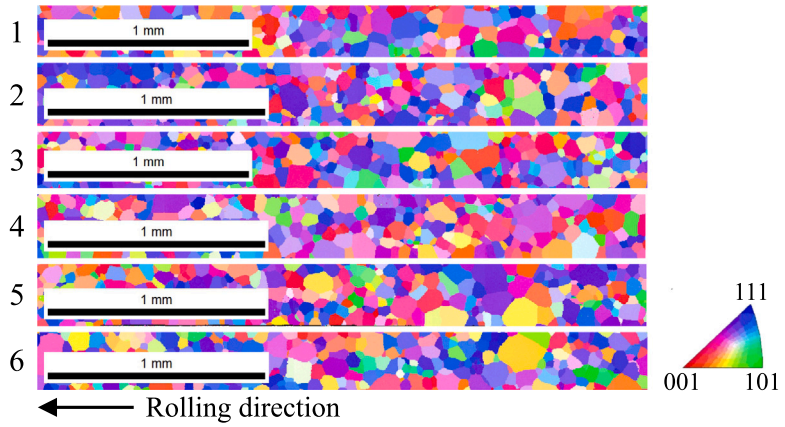

Fig. 3. IPF of six Fe-3%Si samples.

Table 3
Fe-3%Si temperature-dependent mechanical properties at 25 °C and 150 °C. Here the Poisson's ratio η is 0.28 in all the cases.

T [°C]	σ_y [MPa]	σ_{uts} [MPa]	A_g [%]	A_{80} [%]	E_i [GPa]	x_i	r_{x_i}
25	430.10	543.30	18.30	23.60	152	x_1	1.04
25	445.50	566.30	16.77	24.37	162	x_2	1.26
150	326.00	495.00	18.80	25.50	–	x_1	–
150	334.00	538.00	21.20	26.5	–	x_2	–

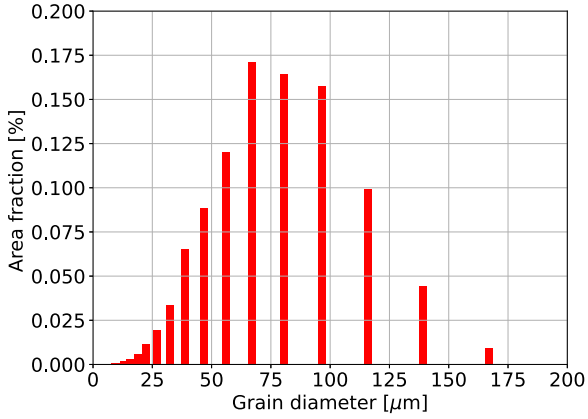

Fig. 4. Grain size fractions of the Fe-3%Si samples.

dependent on the lattice structure. Due to its cubic structure, the single crystal stiffness tensor with three elastic constants in the reduced Voigt notation

$$\begin{bmatrix} C_{11} & C_{12} & C_{12} & \cdot & \cdot & \cdot \\ C_{12} & C_{11} & C_{12} & \cdot & \cdot & \cdot \\ C_{12} & C_{12} & C_{11} & \cdot & \cdot & \cdot \\ \cdot & \cdot & \cdot & C_{66} & \cdot & \cdot \\ \cdot & \cdot & \cdot & \cdot & C_{66} & \cdot \\ \cdot & \cdot & \cdot & \cdot & \cdot & C_{66} \end{bmatrix}, \tag{3}$$

at a known reference coordinate system within the grain. The elastic relationship between global stress $\boldsymbol{\sigma}_i$ and strain $\boldsymbol{\epsilon}_i$ of a single crystal i is

$$\boldsymbol{\sigma}_i = \mathbf{T}_i^{-1}\mathbf{C}\mathbf{T}_i\boldsymbol{\epsilon}_i, \tag{4}$$

for $\mathbf{C}$ the stiffness matrix in single crystal coordinate system x_j', and $\mathbf{T}_i$ the transform matrix from x_j' to the global coordinate system x_j for each grain i (for $i = 1, 2, \ldots N$ grains), calculated as a function of the crystal orientation (see Fig. 6). Thus, by averaging the elastic properties of all grains, one can determine Young's modulus of the overall polycrystal aggregate.

In this work, two average homogenization techniques are used to perform the calculation of the effective elastic properties of polycrystals with cubic and hexagonal lattice systems [12,44,45]. Using Voigt's model that assumes uniform local strains, the overall polycrystal aggregate $\mathbf{C}^V$ is obtained by

$$\mathbf{C}^V = \frac{1}{V_0}\sum_i^{N_g} V_i\mathbf{T}_i^{-1}\mathbf{C}\mathbf{T}_i, \tag{5}$$

for V_i denoting the volume of grain i, V_0 the total volume of the polycrystalline body whose number of grains is N_g, and the transform matrix $\mathbf{T}_i$ is in the function of the crystal orientation. On the other hand, Reuss' model assumes uniform local stress, obtained from

$$\mathbf{S}^R = \frac{1}{V_0}\sum_i^{N_g} V_i\mathbf{T}_i^{-1}\mathbf{S}\mathbf{T}_i, \tag{6}$$

where the single crystal $\mathbf{S} = \mathbf{C}^{-1}$. The V-R volume averaging models correspond to upper and lower bounds to the true behavior, respectively [12,37]. It is then possible to obtain Voigt's $\mathbf{C}^V$ and Reuss' $\mathbf{C}^R$ from the data collected by EBSD, such as crystallographic orientation and area of each grain of the polycrystal. In this case, the volume fraction $V = V_i/V_0$ in Eqs. (5) and (6) is changed by the area $A = A_i/A_0$ fraction of each grain. Once crystallographic orientation given by the EBSD data is obtained on an area of a polished sample. In the end, the anisotropic tensors $\mathbf{C}^V$ and $\mathbf{C}^R$ with nonzero entries are then reduced for the stress plane state as an orthotropic material. As an example, for Voigt's model,

$$\mathbf{C}^V = \begin{bmatrix} C_{11} & C_{12} & 0 \\ C_{21} & C_{22} & 0 \\ 0 & 0 & C_{66} \end{bmatrix}. \tag{7}$$

Experimentally, the polycrystal tensor $\mathbf{C}$ can also be calculated from the engineering constants obtained by the tensile test. In this work, the experimental C_{11}^e and C_{22}^e from polycrystal experimental tensor $\mathbf{C}^e$ were obtained from the stress–strain curve elastic region obtained in the isothermal tensile test at room temperature (25 °C), shown in Fig. 5. The tensor $\mathbf{C}^e$ is not obtained for 150 °C due to the limitation of measuring the specimen strain by the tensile machine. At the end, $\mathbf{C}^V$ and $\mathbf{C}^R$ calculated using Eqs. (4) and (6), are compared to the experimental $\mathbf{C}^e$ in 25 °C to evaluate the precision of each equation.

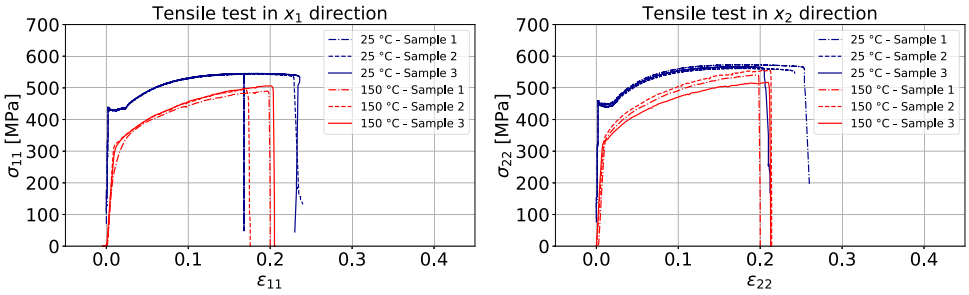

Fig. 5. Fe-3%Si stress–strain curve in x_i directions at 25 °C and 150 °C.

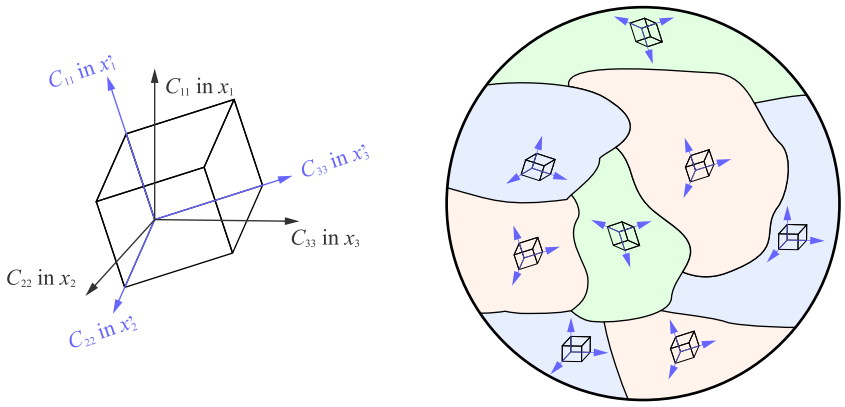

Fig. 6. Distribution of crystalline orientation.

Table 4
Elastic constants of Fe-3%Si single crystal (in units of GPa) [36].

T [K]	T [°C]	C_{11}	C_{12}	C_{44}
300	26.85	236	138	136
0	−273.15	245	140	141

The most accurate equation is chosen to calculate the polycrystalline **C** for different temperatures.

The values of the elastic constants obtained experimentally were $C_{11}^e = 152.00 \pm 1.63$ GPa and $C_{22}^e = 162.00 \pm 3.74$ GPa (Table 3). Table 4 gives the elastic constants as a function of the temperature for a single-crystal of Fe-3%Si with lattice structure $a = 2.8601$ Å [36]. The $\mathbf{C}^V$ and $\mathbf{C}^R$ for ambient temperature was calculated considering 6, 40, 172, 331, 769, 1170, 1548, 1548, 1953, and 2290 grains with their respective crystallographic orientations obtained by EBSD (Table 2).

Fig. 7 shows the comparison between the 11 and 22 components of the V-R calculated $\mathbf{C}^V$ and $\mathbf{C}^R$ tensors, and experimental $\mathbf{C}^e$ at 25 °C for several number of grains. From the Reuss' equation, $C_{11}^R = 136.06$ GPa and $C_{22}^R = 147.53$ GPa. Resulting in a relative error equal to 10.5% and 8.9% in x_1 and x_2 directions, respectively, when compared to experimental results. Furthermore, from the Voigt's equation, $C_{11}^V = 266.47$ GPa and $C_{22}^V = 269.95$ GPa. Resulting in a relative error equal to 75.3% and 66.6% in x_1 and x_2 directions, respectively.

The difference between the limits calculated by the V-R volume averaging models and the experimental results comes from the interactions between the grain boundaries. Even in polycrystals with equiaxed grains, grain boundaries and size imperfections can promote complex interactions that V-R models do not describe. Results are convergent from calculation considering at least 172 grains, and it seems that Reuss' equation calculated $\mathbf{C}^R$ more accurately to the experimental values when compared to Voigt's equation for cold-rolled silicon steels. For this reason, Reuss' equation was chosen to calculate the temperature-dependent elastic constants in the subsequent numerical analyses.

According to the ASME B31.1-2018 [46], the temperature-dependence of low-alloy steels can be described by a linear equation once the modulus of elasticity decays linearly with temperature when the material is not heated to its creep temperature. Low-alloy steel is a metal mixture composed of steel and 1%–5% of alloying elements. Therefore, in this work, estimated values of temperature-dependent **C** of the Fe-3%Si single crystal are assumed for temperatures above 25 °C from values shown in Table 4. Results are shown in Fig. 8.

This model consists in evaluating the anisotropic stiffness tensor C_{ijkl} in the macroscale using the V-R volume averaging model over the polycrystalline structure. This is an initial framework to evaluate the temperature-dependent material properties influence in electric motor rotors thermoelastic behavior. For future analysis, a multi-scale approach needs to be considered to include texture or crystal orientation at a microscopic level throughout the scales e.g. an extension of the computational framework previously proposed in [9,47].

2.5. Coefficient of thermal expansion

When the crystal temperature changes, the resulting deformation is specified by the strain tensor ε_{ij}. For a small and uniform temperature change ΔT throughout the crystal, the deformation is homogeneous, and it is found that all the ε_{ij} components are proportional to θ that represents the change in the temperature $\theta = \Delta T$. Thus,

$$\varepsilon_{ij} = \alpha_{ij}\theta, \tag{8}$$

where the α_{ij} are the coefficients of thermal expansion, for α_1, α_2, and α_3 the thermal expansion coefficients in each main direction x_i. Since Fe-3%Si structures possess cubic symmetry, the linear thermal expansion tensor α_{ij} in a plane stress case is given by

$$\alpha_{ij} = \begin{bmatrix} \alpha_{11} & 0 \\ 0 & \alpha_{22} \end{bmatrix}, \tag{9}$$

where, due to its isotropic thermoexpansion, $\alpha_{11} = \alpha_{22}$. The coefficients of linear thermal expansion (CTE) were experimentally obtained from

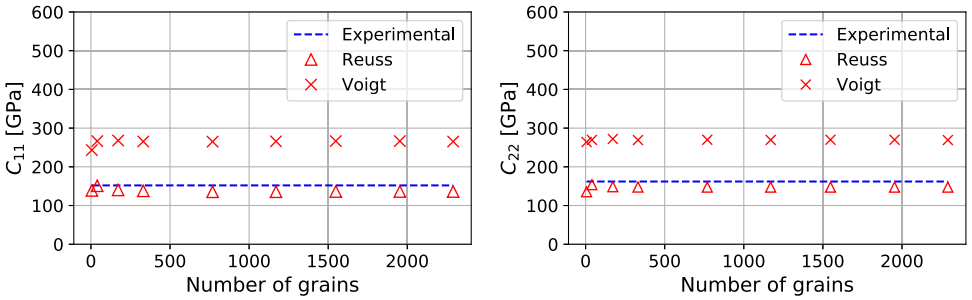

Fig. 7. Comparison between the 11 and 22 components of the calculated $\mathbf{C}^V$ and $\mathbf{C}^R$ tensors, and average values of $\mathbf{C}^e$ at an ambient temperature as a function of the EBSD number of grains considered in the calculation.

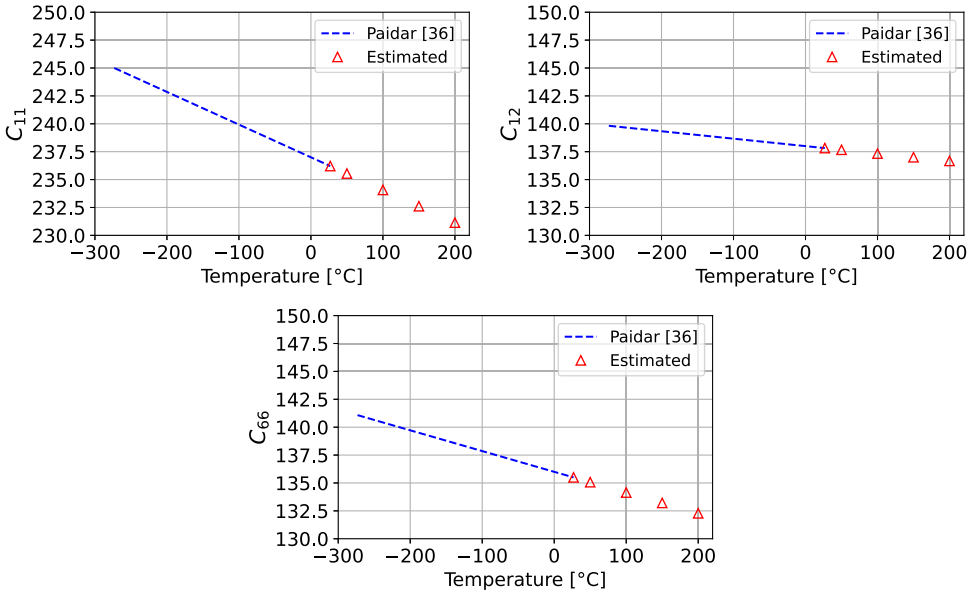

Fig. 8. Single crystal $\mathbf{C}$ estimation of Fe-3%Si.

Table 5
Fe-3%Si coefficient of thermal expansion. SD for Standard deviation.

T [°C]	α_{11} [°C^{-1}]	SD α_{11} [°C^{-1}]	α_{22} [°C^{-1}]	SD α_{22} [°C^{-1}]
26 → 200	1.08×10^{-5}	4.64×10^{-7}	1.01×10^{-5}	3.24×10^{-7}

Table 6
Fe-3%Si thermal conductivity. SD for Standard deviation.

T [°C]	κ [W/mK]	SD [W/mK]
25	21.72	0.26
50	23.61	0.31
100	22.18	0.25
150	29.1	0.37

DIL 402PC NETZSCH® dilatometer according to ASTM E228-17 standard [30] in a temperature range from 26 °C to 200 °C. The test was performed in the global coordinate system's x_1 and x_2 directions in 8 × 4 mm samples.

Table 5 shows the results for α_{ij}. It is not possible to determine the degree of anisotropy of the thermal expansion coefficient because, statistically considering the standard deviation, the coefficients are equal in both directions. Therefore, it is assumed that $\alpha_{11} = \alpha_{22} = 1.04 \times 10^{-5}$ °C^{-1}. i.e., it is assumed that the cold-rolled silicon steel is isotropic regardings the coefficient of thermal expansion.

2.6. Thermal conductivity

Thermal conductivity is the material's capacity to conduct or transfer heat. The Fe-3%Si alloy thermal conductivity was experimentally measured by the Modified Transient Plane Source (MTPS) technique according to ASTM D7984 16 [27] by the C-Therm® equipment. The rise in temperature at the interface between the MTPS sensor and specimen induces a voltage drop in the sensor. The rate of increase in the sensor voltage is directly informed by C-Therm® equipment and is used to determine the effusivity b. The thermal conductivity κ is then calculated by:

$$b = (\kappa \varrho c_p)^{1/2}, \tag{10}$$

for c_p being specific heat and ϱ the material's density. In this work, a cylindrical Fe-3%Si alloy sample was taken before the continuous casting process. The sample was pressed against the sensor with a weight equivalent to 50 g, and seven measurements were done. The sample was heated until stabilization in target temperatures with a tolerance of ±2 °C. The target temperatures tested were 25, 50, 100 and 150 °C. The thermal conductivity is given in W/mK. The thermal conductivity κ is shown in Table 6. It is observed that the κ temperature dependence is considerable, and then it cannot be neglected.

The increase in the thermal conductivity coefficient with an increment in temperature is expected for steel alloys. Similar results are shown in [29,48]. Therefore, it is assumed that κ is temperature-dependent.

3. Thermoelasticity formulation

This work implements an uncoupled stationary state formulation to solve the thermoelasticity for plane stress cases considering temperature-dependent material properties. Since physical variables are independent of time, the steady-state heat conduction governed by Laplace differential equations is solved first, whose solution yields the temperature distribution inside the body. The elastic solution is then obtained by calculating the thermal expansion caused by the temperature field previously calculated. Part of the formulation is contained in the database, the link is provided in the Data availability section.

3.1. Elastic representation formulation

This research is based on the boundary element formulation described in [2] that uses the well-known boundary integral equation (BIE), to treat 2D elasticity problems physically described by continuum mechanics and infinitesimal strain theory using the following equations

$$\frac{\partial \sigma_{ij}}{\partial x_j} + \varrho b_i = 0, \quad \varepsilon_{ij} = \frac{1}{2}\left(\frac{\partial u_i}{\partial x_j} + \frac{\partial u_j}{\partial x_i}\right), \tag{11}$$

where σ_{ij} are the mechanical stresses within the solid. The total strain tensor ε_{ij} which is valid for small strain, is a function of the displacement u_i. Here b_i is an inertial load and ϱ is the material density. For a generally anisotropic two-dimension model, the constitutive relationship between the stress σ_{ij} and the mechanical strain considering temperature changes $\theta = T - T_0$ from a reference temperature T_0 is governed by

$$\sigma_{ij} = C_{ijkl}\varepsilon_{ij} - \gamma_{ij}\theta, \tag{12}$$

where C_{ijkl} is the material stiffness coefficients, and γ_{ij} is the thermoelastic tensor given by $\gamma_{ij} = C_{ijkl}\alpha_{kl}$, for α_{ij} being the coefficients of linear expansion. Substituting the Eq. (12) into (11) and considering a static thermoelasticity case where all physical variables are independent of time, the field equation of thermoelasticity is obtained in terms of displacements u_i

$$C_{ijkl}u_{k,lj} - \gamma_{ij}\theta_{,j} + \varrho b_i = 0. \tag{13}$$

The BIE in the direct BEM formulation for a 2D anisotropic solid, when the temperature change θ or and its gradient $\theta_{,j}$ are previously known on the boundary, provides an integral relation between tractions t_i and displacements u_i on the boundary Γ of the domain Ω. Hence, following the procedure described in [2], after some manipulation of Eq. (13) using the principle of virtual work and the Somigliana's identity, the thermoelastic BIE representation formula is given by

$$\begin{aligned} c_{ij}u_j(\xi_i) + \int_\Gamma T_{mi}u_i d\Gamma = \int_\Gamma U_{mi}t_i \\ + \int_\Gamma U_{mi}\gamma_{ij}\theta n_j d\Gamma - \int_\Omega f_i^{el}U_{mi}d\Omega, \end{aligned} \tag{14}$$

for

$$f_i^{el} = \gamma_{ij}\theta_{,j} - \varrho b_i. \tag{15}$$

In the Eqs. (14) and (15), the term $c_{ij} = \delta_{ij}/2$ for a source point ξ_i located on a smooth part of the surface boundary, where δ_{ij} is the Kronecker delta. T_{mi} and U_{mi} are the fundamental solutions for tractions and displacements explained in Appendix A of the complementary formulation. The displacements u_i and tractions t_i are computed on the surface Γ.

The volume integral in the right-hand side of the Eq. (14) needs to be transformed into a boundary integral to restore the distinctive feature of the BEM as a boundary solution computational technique. The dual reciprocity formulation technique (DRBEM), proposed by [49], was used to solve the volume integral for inertial loads, see Appendix B of the complementary formulation. For cases when there is a heat flux in the domain, the domain integral for the thermoelastic therm is transformed to boundary integral by Radial Integration Method (RIM) [50], see Appendix C of the complementary formulation.

3.2. Thermal representation formulation

The steady-state heat conduction is governed by Laplace Differential equations in solids without internal energy generation. Therefore, for θ being change in the temperature,

$$\theta_{,ii} = 0. \tag{16}$$

The authors in [2,51] provide the thermal representation formulation to solve the steady-state conduction without internal energy generation via BEM. From Green's second identity and supposing θ^* as the temperature fundamental solution in a similar manner to the elasticity formulation, we obtain the following equation

$$-\int_\Omega \theta^*_{,ii}\theta \, d\Omega = \int_\Gamma \theta^*\theta_{,i}n_i \, d\Gamma - \int_\Gamma \theta\,\theta^*_{,i}n_i \, d\Gamma. \tag{17}$$

In order to obtain an equation that does not have domain integrals, the function $\nabla^2\theta^*$ is chosen adequately so that the domain integral of Eq. (17) is equal to 0. The function that satisfies this requirement is the function whose Laplacian is the Dirac delta

$$\theta^*_{,ii} = -\frac{\delta(x_i - \xi_i)}{\kappa}, \tag{18}$$

this definition in (18) corresponds to the so called fundamental problem where in an infinite medium the solution θ^* is the fundamental solution, see more details in Appendix D of the complementary formulation. The term x_i is the field point, ξ_i is the source point, and κ is the thermal conductivity. Given the heat flux equation

$$q_i = -\kappa\,\theta_{,ii}. \tag{19}$$

Substituting (18) and (19) into (17) gives

$$\int_\Omega \frac{\delta(x_i - \xi_i)}{\kappa}\theta \, d\Omega = \int_\Gamma \theta^*\frac{q_i}{-\kappa}n_i \, d\Gamma - \int_\Gamma \theta\frac{q_i^*}{-\kappa}n_i \, d\Gamma, \tag{20}$$

resulting by the sifting property being applied in the domain integral in

$$c\,\theta(\xi_i) = \int_\Gamma \theta\, q^* \, d\Gamma - \int_\Gamma \theta^* q \, d\Gamma, \tag{21}$$

for ξ_i being coordinates of a source point, and c being used to take care of several special cases that can arise depending on the location of the source point. i.e., when ξ_i is inside the domain, c equals 1. When ξ_i is on the boundary, c is equal to either $-1/2$ for smooth boundary points. From Eq. (21), the temperature and flux fields are evaluated as scalers at each node of the boundary elements, where the flux q is given directly at the normal direction of the surface.

3.3. Uncoupled thermoelastic solution

According to [2], the uncoupled thermoelastic equation is obtained by combining the Eqs. (14) and (21) is

$$\begin{aligned} \begin{bmatrix} c_{ij}u_m(\xi_i) \\ c\,\theta(\xi_i) \end{bmatrix} = \int_\Gamma \left\{ -\begin{bmatrix} t^*_{mi} & -u^*_{mi}\gamma_{ij}n_j \\ 0 & -q\,* \end{bmatrix}\begin{bmatrix} u_i \\ \theta \end{bmatrix} + \begin{bmatrix} u^*_{mi} & 0 \\ 0 & -\theta^* \end{bmatrix}\begin{bmatrix} t_i \\ q \end{bmatrix}\right\} d\Gamma \\ - \int_\Omega \begin{bmatrix} u^*_{mi} & 0 \\ 0 & 0 \end{bmatrix}\begin{bmatrix} f_i^{el} \\ 0 \end{bmatrix}. \end{aligned} \tag{22}$$

Nonetheless, in the case of static thermoelasticity, it is possible to solve by an uncoupling solution where: first, the Eq. (21) is solved to obtain the temperature field θ. Then, the solution of the elastic equation is straightforward by the thermal coupling therms $\gamma_{ij}\theta$ and $\gamma_{ij}\theta_{,j}$ in Eq. (14). This is possible because all variables are time-independent.

In this work, the implementation was carried out using FORTRAN 90 language. The equations were discretized using discontinuous

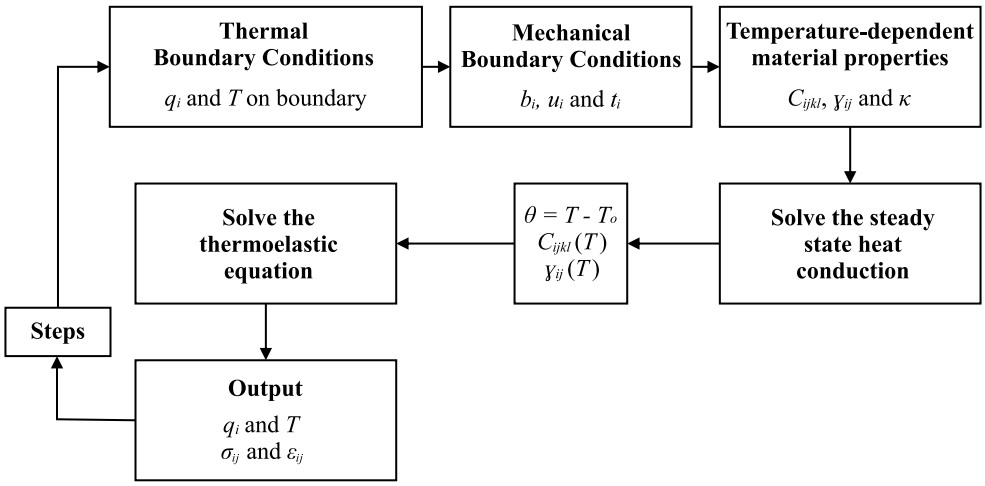

Fig. 9. Flowchart of uncoupled thermoelastic solution.

quadratic elements to discretize the boundaries, for more details of the type and formulation of different boundary elements see [51]. Fig. 9 shows the code structure. First, the following information is entered as input: temperature-dependent material properties, number of step analysis, and the boundary conditions q, T, u_i, and t_i for each step. At first, the steady-state heat conduction is solved by providing θ for each node. Then, the elastic constants C_{ijkl} and the thermoelastic tensor γ_{ij} are defined as a function of body temperature calculated by the Reuss' averaging method. The thermoelastic tensor γ_{ij} is also obtained in the function of the body temperature. Finally, the thermoelastic problem is solved for each step analysis, providing the displacements, strains, and stresses.

The formulation presented here is validated throughout several examples contained in the database, see the Data availability section. With an anisotropic elastic and thermal properties of Fe-3%Si, the following test were successfully run: (i) sheet under its own weight, (ii) thermoelastic problem with inertial forces in a classic beam, (iii) beam subjected to a quadratic thermal load, (iv) beam subjected to a linear thermal load. In this work, the exact and FEM solutions are used only for validation purposes. However, the advantage of using BEM is that the secondary response of the internal points such as in the is more accurate as the internal point can be located exactly in the desired position. Also, it is well-known that BEM is useful for high gradients solutions.

4. Analysis of the degradation of the material strength

One industrial application where these steels are highly employed is in the rotors of electrical motors, as they provoke severe operational conditions. Therefore, the high rotational speeds infer considerable stresses due to inertial loads on the rotor [19,20]. The radial displacements and stresses calculation is paramount in the design of electric motor rotors. The stresses must be understood if yield or fatigue failure criteria are applied. On the other hand, the maximum radial displacement must be known so that the thermal expansion or deformation by centrifugal inertial loading is not greater than or equal to the air gap. If the radial deformation exceeds the air gap, the rotor can touch the stator, causing a mechanical failure due to the impact. The air gap is the distance between the rotor and the stator. According to [52], the smaller the air gap, the smaller the magnetic flux resistance to cross the space between the rotor and stator since the relative permeability of the air is lower than in the ferromagnetic medium.

There are works that have shown cases in which a null temperature gradient was obtained along the radial length in the rotor [31,32], i.e., it can be assumed that the rotor temperature is equal at all points in the rotor. The temperature values change during operation once the part is heated by induction. In addition, the electric motor can operate at constant speed or variable speed. Both thermal and inertial loads promote stresses, strains, and displacements in the rotor.

Table 7
Fe-3%Si temperature-dependent properties. $\mathbf{C}^R$ for Fe-3%Si single crystal.

Constant	Value or equation	Unit
C_{11}	$-0.030(T) + 236.99$	GPa
C_{12}	$-0.0066(T) + 137.99$	GPa
C_{66}	$-0.019(T) + 136.044$	GPa
α_{11}	1.04×10^{-5}	$°C^{-1}$
α_{22}	1.04×10^{-5}	$°C^{-1}$
k	$781.15 - 67.78(T) + 1.58(T^2)$	W/mK

Recent studies show application analyses of the Fe-3%Si alloy under these conditions considering the material temperature-dependent elastic properties. However, the mechanical properties are not presented in greater detail, or the mechanical properties are assumed as isotropic, and in most of them, these thermal effects are neglected. Therefore, a synchronous topology rotor of Fe-3%Si steel is subjected to variable combinations between rotation and temperature loads. The elastic constants are temperature-dependent and calculated by the Reuss' model, and all the mechanical and thermal properties are defined according to as shown in Section 2. Ultimately, the temperature effect on radial displacements and stresses is calculated, analyzed, and discussed. In addition, the temperature influence on yield failure criteria is presented. The Fe-3%Si properties considered in this analysis are condensed in Table 7. Where the orthotropic C_{ijkl} is calculated from the temperature-dependent elastic constants of the single crystal using the reduced Voigt notation C_{11}, C_{12} and C_{66}, and EBSD by Reuss' equation following the methodology shown in Section 2.4.

4.1. Geometry and boundary conditions

This work considers a general geometry of a rotor with a synchronous topology of 80 mm of external diameter. Due to the rotor axisymmetry, which its C_{ijkl} is modeled as orthotopic with material orientation axes $(1, 2)$ is coincident to the geometrical rotor (x_1, x_2) axes, the tensor of elastic properties using the reduced Voigt notation is

$$\mathbf{C}^R(T) = \begin{bmatrix} C_{11} & C_{12} & 0 \\ C_{21} & C_{22} & 0 \\ 0 & 0 & C_{66} \end{bmatrix}. \tag{23}$$

Here, simulations are carried out under the plane stress condition. Further, it is modeled in a 1/4 model under centrifugal forces and thermal loads according to Fig. 10.

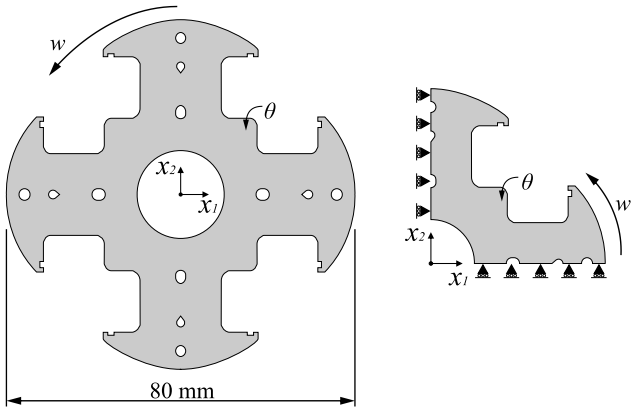

Fig. 10. A Synchronous topology of the electric motor rotor under centrifugal forces and thermal loads.

Table 8
Thermal and inertial loading combinations per analysis step.

Step	ω is constant		θ is constant	
	θ [°C]	ω [RPM]	θ [°C]	ω [RPM]
1	0.00	20000	150.00	1000
2	25.00	20000	150.00	2500
3	30.00	20000	150.00	5000
4	50.00	20000	150.00	7500
5	62.50	20000	150.00	10000
6	75.00	20000	150.00	12500
7	87.50	20000	150.00	15000
8	100.00	20000	150.00	17500
9	112.50	20000	150.00	20000
10	125.00	20000	–	–
11	137.50	20000	–	–
12	150.00	20000	–	–

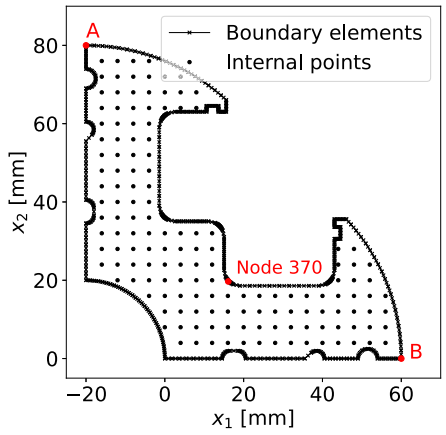

Fig. 11. Mesh with 320 quadratic boundary elements and 151 internal points. Some points or nodes are highlighted to be analyzed in the next subsections.

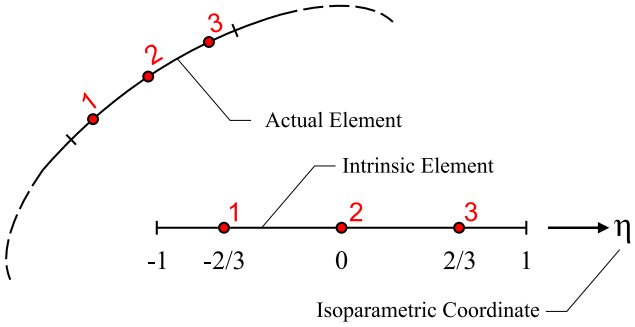

Fig. 12. Quadratic discontinuous boundary element.

Once the fundamental solutions for anisotropic elastic problems are dependent on the material elastic constants S_{ijkl}, the only option to consider the temperature dependence on the material is to assume that the temperature is uniform throughout the body for each step analysis, as shown by [31,32]. About the ω and θ boundary conditions considered in this analysis, two load cycles are imposed: the first keeps the rotation ω constant at 20 000 RPM, changing the temperature variation θ from 0 to 150 °C in 12 steps. The second condition keeps the temperature variation θ constant at 150 °C, changing the rotation ω from 1000 to 20 000 RPM in 9 steps, see Table 8.

Therefore, it will be considered in this example that the temperature changes in each step of the analysis, and there is no heat flux in the domain. In addition, the inertial load will be defined as the function of angular velocity ω changing in each step analysis, described by the Newtonian mechanics' equation

$$b_i = \rho\omega^2 x_i, \tag{24}$$

this equation is applied for centrifugal loads on rotating disks as used before in [53–55]. This force appears on all objects in a rotating frame of reference.

4.2. Mesh and convergence analysis

Discontinuous quadratic boundary elements and equidistant internal points were used to discretize the geometry. A mesh convergence analysis was carried out considering θ = 150 °C and ω = 20 000 RPM as boundary conditions. The mesh convergence error was calculated as a relative error for each new result in the current mesh about the previous mesh. Four mesh refinement steps were necessary to achieve convergence, resulting in a relative error of 0.17% for the maximum σ_{11} and 0.006% for the maximum total displacement u_t, given by

$$u_t = \sqrt{(u_1)^2 + (u_2)^2}. \tag{25}$$

The final mesh has 320 boundary elements and 151 internal points, shown in Fig. 11.

At the contour, the elements are composed of three nodes inside the proper element, and they are mapped on an intrinsic space using quadratic shape function, see Fig. 12. More details about how to formulate and discretize the equations in [56].

Finally, the internal points are simple nodes located within the domain with coordinates x_i.

4.3. Results

The total displacement u_t is shown in Fig. 13 for four boundary conditions. Comparing the results at θ = 25 °C considering a first case with ω = 1000 RPM and a second case for ω = 20 000 RPM, the maximum u_t has increased from 0.022 mm to 0.0238 mm, and this is an 8.18% increment of u_t in displacement. Comparing the results at ω = 20 000 RPM and changing the thermal variation θ from 25 °C to 150 °C, the maximum u_t has increased from 0.0238 mm to 0.134 mm, resulting in a 463.02% increment of u_t. Similar behavior is observed in the other possible loading combinations.

It is observed that the displacements are equal in all conditions, where they occur mainly in the radial direction. Also, the thermal load is homogeneous, causing a purely volumetric thermoelastic expansion. The inertial loading acts primarily in the radial direction of the body and provides a small component in the displacement compared to the thermoelastic displacement components.

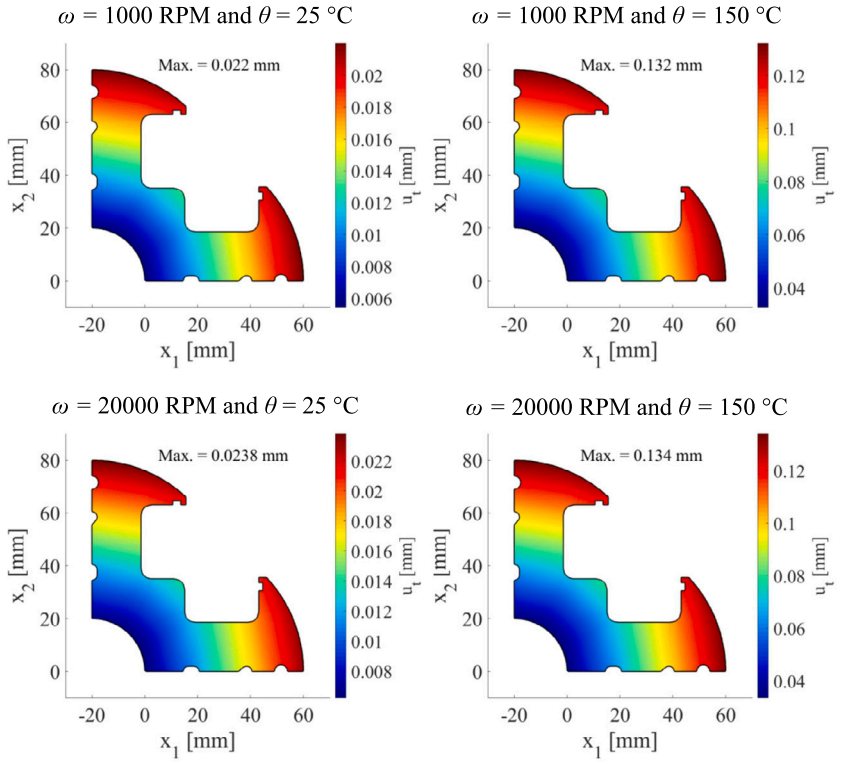

Fig. 13. Rotor u_t for four load combinations.

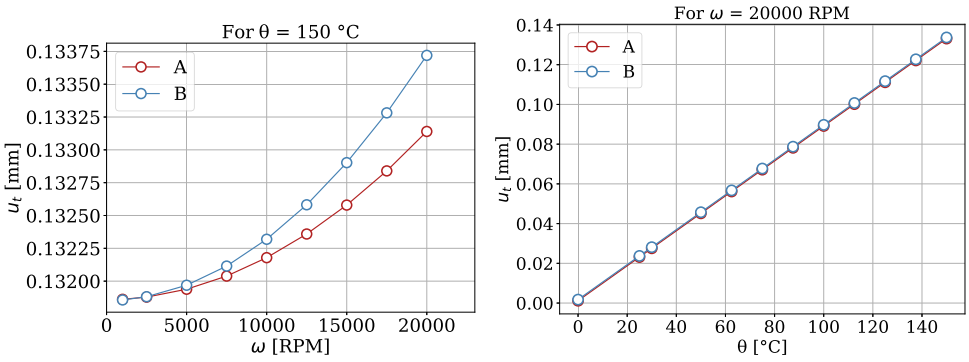

Fig. 14. Maximum displacement variations at A and B points for the results for uniform temperature change θ, and constant rotation ω.

Fig. 14 shows the maximum total displacements at A and B points, see Fig. 11. It is observed that the increment of the rotation ω at a constant temperature θ increases the displacement difference between A and B points in the radial direction. It happens due to the anisotropy once the inertial load acts directly in the body force b_i term. The maximum difference in u_t between A and B points is 0.57942×10^{-3} mm. It is also observed that the increment in displacement is a function of the rotation that follows a quadratic behavior. This is due to the quadratic term of the inertial loading in Eq. (24).

It is also shown in Fig. 14 the maximum radial displacements for a constant rotor rotation ω at different temperature changes θ. In a fixed rotor rotation, these changes do not increase the difference in the displacements of the A and B points. The difference in u_t at all points is equals 0.57942×10^{-3} mm once $\theta = 150$ °C. It happens because the tensor α_{ij} is isotropic, and the thermal expansion component of displacement is greater than the inertial component. For uniform $\theta =$ 150 °C and ω changing from 1000 to 20 000 RPM, the u_t increased from 0.13186 mm to 0.13372 mm at point B. While for constant $\omega =$ 20 000 RPM and θ changing from 25 to 150 °C, the u_t increased from 0.00175 mm to 0.13372 mm at point B. Therefore, since α_{ij} is isotropic, the displacements will purely depend on the elastic constants C_{ijik}, which depend on the polycrystal texture and grain size.

The stress components for the same four boundary conditions are shown in Figs. 15–17. Comparing the results at $\theta = 25$ °C and increasing the rotor rotation ω from 1000 RPM to 20 000 RPM, the maximum σ_{11} increased from 0.64 MPa to 256.55 MPa, σ_{22} increased from 0.66 MPa to 264.63 MPa, and σ_{12} increased from 0.23 MPa to 93.61 MPa. Resulting in a significant increase in all the stress components due to inertial loading increment. A difference of 8.08 MPa between the maximum values of σ_{11} and σ_{22} is also observed, caused by the orthotropy of C_{ijkl}. Nonetheless, comparing the results at $\omega =$ 20 000 RPM and changing the thermal variation θ from 25 °C to 150 °C, the components σ_{11}, σ_{22}, and σ_{12} do not change. Since the thermoelastic expansion is purely volumetric and there are no supports in the rotor boundary condition to resist this expansion, the thermoelastic stress components are zero. Similar behavior occurs in the other possible loading combinations.

A node in a region of geometric discontinuity was chosen to analyze the variation in stresses. Fig. 18 shows the maximum variations of stress

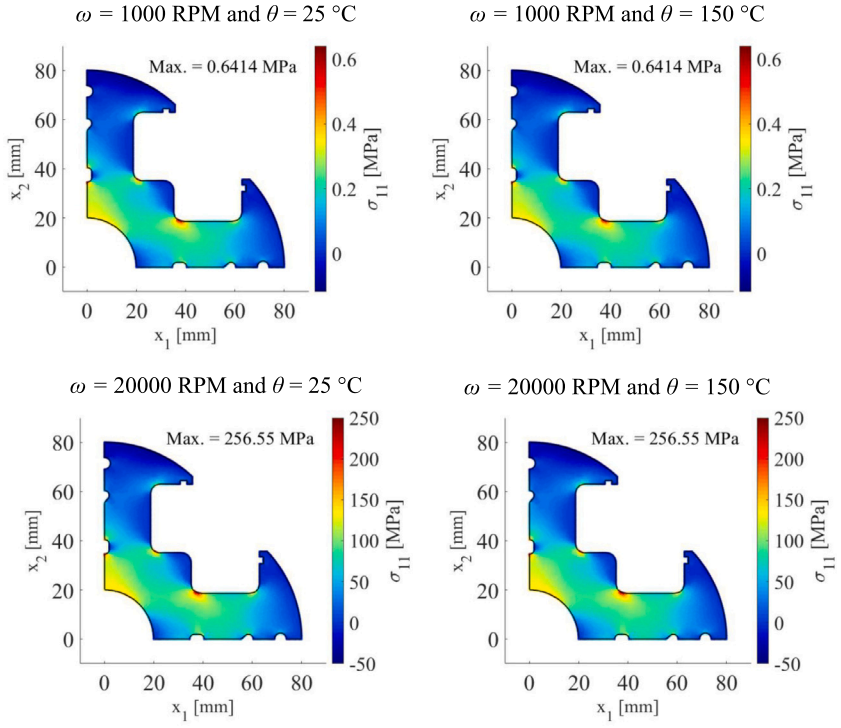

Fig. 15. Rotor σ_{11} for four load combinations.

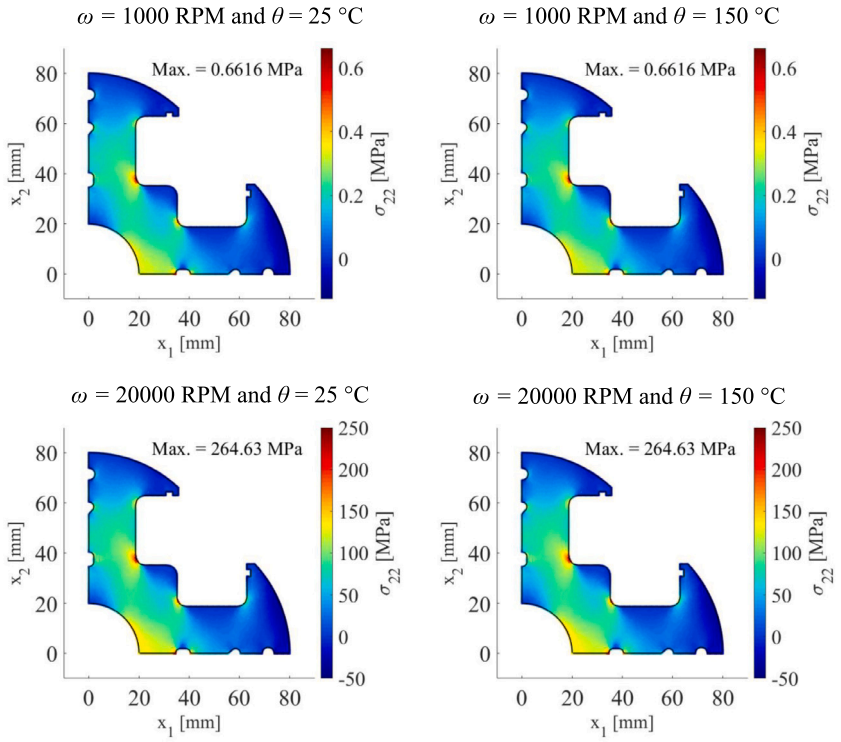

Fig. 16. Rotor σ_{22} for four load combinations.

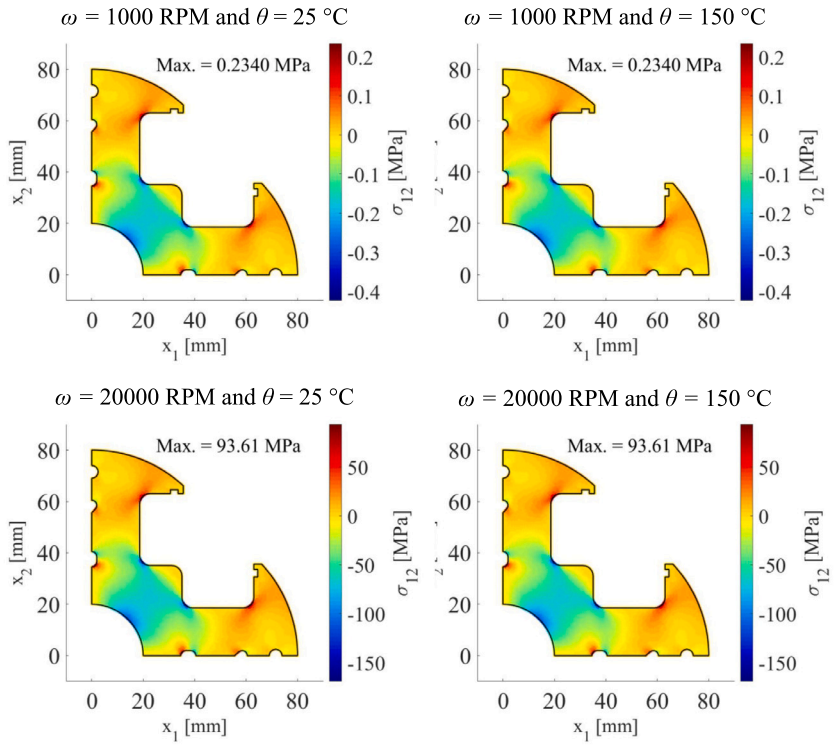

Fig. 17. Rotor σ_{12} for four load combinations.

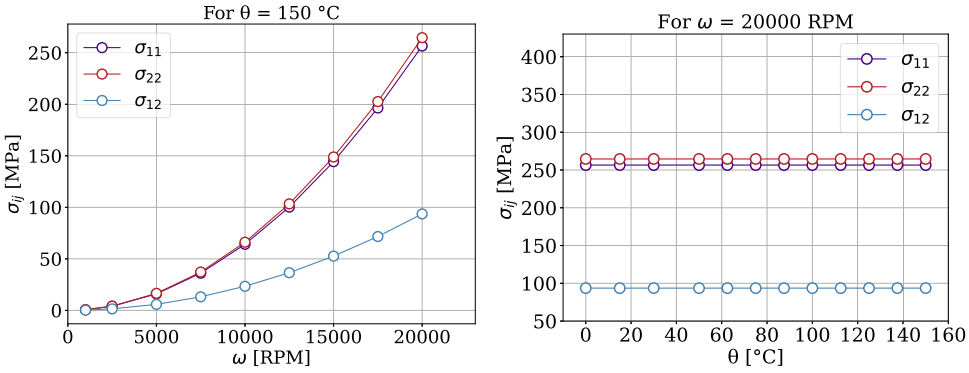

Fig. 18. Stress components variations at node 370 for uniform temperature and constant rotation.

components as a function of rotor rotation or temperature change at node 370, see Fig. 11. A stress increment in a quadratic response was observed for an increasing ω at a uniform $\theta = 150$ °C. Similar to radial displacements, it happens due to the quadratic load $b_i = \rho\omega^2 x_i$. It is also observed that the stress components do not increase with the increment of the temperature.

Although the temperature increment does not increase the stresses for this case, they could increase for other applications such as cantilevered supports, bonded surfaces, contacts with other parts made of different materials, or temperature gradients changed as a function of thermal loading.

4.4. Failure criterion

A failure criterion is analyzed for the case of study presented here, where the temperature effect in mechanical failure is evaluated. For this purpose, given the Fe-3%Si anisotropic properties, a yield criterion proposed in [23] to evaluate rolled sheets of polycrystalline metal where the texture is fine-grained is applied. Each macro-element of material is treated as homogeneous and structurally orthotropic. The equations of this criterion are proposed to allow this evaluation from the experimental data obtained by tensile test and stress components numerically calculated.

Given that σ_b is the yield stress of a thin sheet under in-plane equibiaxial tension, and σ_{x_1} and σ_{x_2} are the yield stress under uniaxial tension at 0° and 90° to the rolling direction, respectively. This criterion proposes that when σ_{x_1} and σ_{x_2} are distinct, the yield function is given by

$$\mathcal{N} = \frac{\sigma_{11}^2}{\sigma_{x_1}^2} - \frac{c\sigma_{11}\sigma_{22}}{\sigma_{x_1}\sigma_{x_2}} + \frac{\sigma_{22}^2}{\sigma_{x_2}^2} + \left\{(p+q) - \frac{(p\sigma_{11} + q\sigma_{22})}{\sigma_b}\right\}\frac{\sigma_{11}\sigma_{22}}{\sigma_{x_1}\sigma_{x_2}} \tag{26}$$

where σ_i and σ_{x_i} are temperature-dependent, and p, q, and c are parameters defined by the equations shown in [23] based on Lankford coefficients r_0 and r_{90}. The yield failure occurs when the left-hand side $\mathcal{N}$ of Eq. (26) is bigger than 1. I.e, $\mathcal{N} > 1$ denotes failure. In this analysis, σ_b is assumed as:

$$\sigma_b(T) = \frac{\sigma_{x_1}(T) + \sigma_{x_2}(T)}{2}. \tag{27}$$

and σ_{x_1}, σ_{x_2}, r_0, and r_{90} given in Table 9.

Table 9
Fe-3%Si temperature-dependent properties.

Constant	Value or equation	Unit
σ_{x_1}	$-0.8328(T) + 450.92$	MPa
σ_{x_2}	$-0.892(T) + 467.80$	MPa
r_0	1.08	–
r_{90}	1.25	–

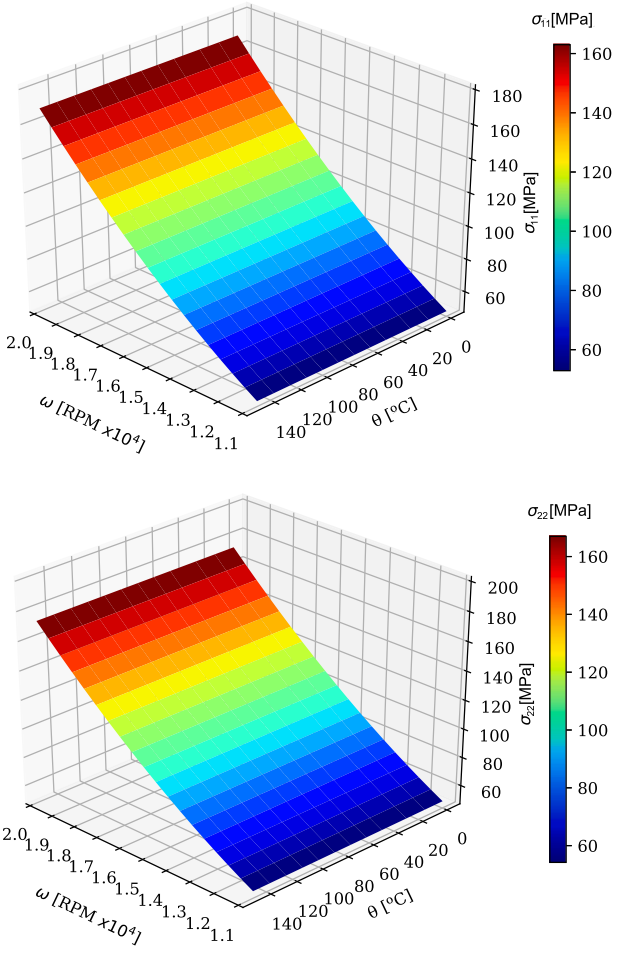

Fig. 19. Loadings ω and θ effects on σ_{11} and σ_{22}.

Fig. 19 shows the stress components σ_{11} and σ_{22}, only for the node 370 shown in Fig. 11, for several thermal and inertial load combinations where ω goes from 11 000 RPM to 20 000 RPM and θ from 0 to 150 °C. Allowing to evaluate the increment of the rotor normal stresses at this point as a function of increasing rotor speed and temperature, understanding its effects before calculating $\mathcal{N}$.

The rotor stress components σ_{11} and σ_{22} do not increase with the temperature variation θ increment and increase in a quadratic response as a function of ω. The σ_{11} and σ_{22} are stress components parallel and perpendicular to the rolling direction, respectively. As the temperature reduces the yield strength of the Fe-3%Si steel, the increment of the temperature reduces the yielding limit or maximum stress resistance. Therefore, despite no increase in the stress components, the temperature change cannot be neglected in the design or analysis of mechanical components.

To evaluate the material response to the temperature load, Eq. (26) is applied at each stress point in Fig. 19 calculated for all combinations of σ_{11} and σ_{22} as a function of θ and ω, considering all the temperature-dependent Fe-3%Si properties shown in Tables 7 and 9. The resulting $\mathcal{N}$ for each load combination at node 370 is shown in Fig. 20.

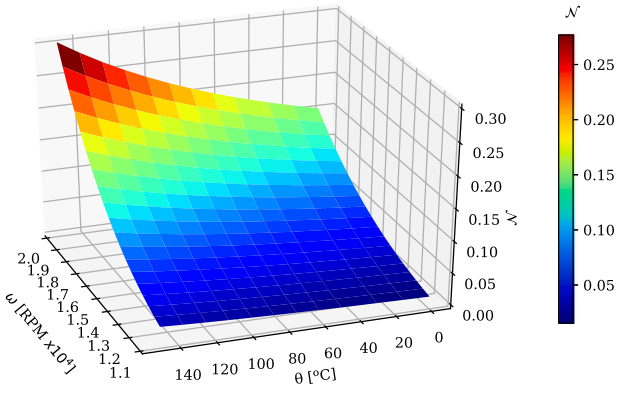

Fig. 20. Effects of inertial and thermal loads on $\mathcal{N}$.

It is observed in Fig. 20 that, despite the temperature load does not increase the rotor stresses as shown in Fig. 19, the temperature increment reduces the yield strength σ_y and, consequently, increases the $\mathcal{N}$. i.e., the temperature increment approximates the part to a failure condition even in cases with constant rotation ω reducing the material yield strength. The quadratic response with the temperature increment is directly related to Eq. (26). Therefore, for this case, this approximation to a failure condition is directly related to rotation increment and the decrease on σ_y for x_i directions with the temperature increment. These effects of temperature are especially critical at operating points that combine high speed and high temperature.

Since the temperature increment reduces the mechanical properties of the alloy, the design must consider the influence of temperature on its elastic constants and the effect of temperature on the plastic constants if failure criteria or other studies consider plasticity. In this case, the temperature increment from 25 to 150 °C increased $\mathcal{N}$ from 0.149 to 0.300 at maximum rotation ω = 20 000 RPM, a growth of 101.61%. In cases where the temperature increment changes σ_i, this increase in $\mathcal{N}$ can be more significant by adding stress increasing as a function of temperature load. Isothermal experiments could be performed on a motor test bench, or using a biaxial tensile test machine to check the approach accuracy. In both cases, the apparatus needs to be capable of controlling the prototype or sample temperature.

5. Conclusions

The uncoupled thermoelastic phenomenon in cold-rolled silicon steels subjected to severe thermal and inertial loads was analyzed, taking into account the influence of temperature on its mechanical, elastic, and thermal properties. A small error value magnitude between BEM, exact, and FEM solutions indicated that the BEM pointed out a good performance. Furthermore, a procedure was presented to deal with the temperature-dependent elastic properties homogenization of cold-rolled silicon steel with 3.3%Si from EBSD data, obtained experimentally at the microscale, by Reuss' equation. It is observed that Reuss' equation is more efficient in calculating the temperature-dependent elastic constants for cold-rolled Fe-3%Si. In addition, the main thermal elastics properties of a Fe-3%Si alloy and its grains' crystallographic orientations and morphology by the EBSD technique are presented in this work. The data collected can be used in future works to evaluate elastic properties homogenization by numerical methods, crack propagation analysis, and atomistic studies.

It has been demonstrated how these materials are sensitive to ambient conditions that can affect their resistance and in particular for the application mentioned here, a thermal analysis in a synchronous rotor topology showed the inertial and thermal influences on the rotor radial displacements, stresses, and yield limit. However, it would be possible to consider other scenarios where similar characterizations

are required for future design recommendations. For this research, a yield criterion proposed in [23] to evaluate rolled sheets of polycrystalline metal where the texture is fine-grained demonstrated that the influence of temperature and inertial loads due to operation on the mechanical properties of the Fe-3%Si alloy is considerable. Even in applications where thermal loading does not change the stress distribution, the increase in the temperature considerably reduces the mechanical strength. Therefore, the temperature dependence must be considered in all the Fe-3%Si alloy mechanical and elastic properties during the design or analysis. Furthermore, the constant of thermal expansion and κ can be assumed as isotropic, while the mechanical properties must be considered orthotropic, this is a remarkable conclusion compared with previous analyses of synchronous rotors in the literature.

In summary, the framework proposed in this work shows the thermal load influences in synchronous electric rotors failure and thermoelastic behavior. Generally, these influences are commonly despised or not completely understood by literature or industrial electric rotors works [19–22]. From a good understanding of how much thermal loadings contribute to rotor radial displacement, smaller air gaps can be proposed in new electric motor designs to reduce the magnetic flux resistance in these regions. Finally, considering the influence of temperature in the failure criteria ensures that rotor failure prediction is more accurate.

CRediT authorship contribution statement

Caio Moura: Investigation, Methodology, Software, Validation, Visualization, Writing – original draft. **Andres F. Galvis:** Conceptualization, Writing – review & editing, Supervision. **Paulo Sollero:** Conceptualization, Supervision, Funding acquisition.

Declaration of competing interest

The authors declare that they have no known competing financial interests or personal relationships that could have appeared to influence the work reported in this paper.

Data availability

The supplementary material of these findings and results are available to download from http://dx.doi.org/10.17632/d24fmr56db.1. This database contains results of Fe-3%Si cold-rolled silicon steel characterizations. There are folders containing Electron Backscatter Diffraction (EBSD), tensile tests at 25 and 150 °C, and X-ray diffraction results available. For EBSD data, there is information about the crystallography directions and grain sizes. For tensile tests at 25 and 150 °C, there are the strain-stress curves, and for X-ray diffraction, there are the data to get the diffraction graph and scan parameters. Finally, complementary formulation, numerical validations, and interactive plots are included providing a better resolution of all the graphs and plots shown in this paper.

Acknowledgments

The authors would like to thank the University of Campinas (Brazil) and the University of Portsmouth (UK) for the facilities and structure provided to develop this work. The project was funded by the Brazilian Coordination for the Improvement of Higher Education Personnel-CAPES (Grant Number: 435214/2019-01). This material is based on work supported by the Air Force Office of Scientific Research-AFOSR, United States under Award Numbers FA9550-18-1-0113 and FA9550-20-1-0133.

References

[1] J. Salençon, Handbook of Continuum Mechanics: General Concepts Thermoelasticity, Vol. 1, Springer, 2001.
[2] L. Gaul, M. Kogl, M. Wagner, Boundary Element Methods for Engineers and Scientists, Vol. 1, Springer, 2003.
[3] D. Ieşan, Thermoelastic Models of Continua, Vol. 1, Springer, 2004.
[4] A. Franke, J. Schneider, B. Bacroix, Evolution of microstructure and texture in ferritic FeSi steels at final annealing – role of strain induced boundary migration and secondary recrystallization, in: HAL (Ed.), International Conference Magnetism and Metallurgy WMM20, Vol. 9, Rome, Italy, 2020, p. 349.
[5] A.F. Galvis, R.Q. Rodriguez, P. Sollero, E.L. Alburquerque, Multidomain formulation of BEM analysis applied to large-scale polycrystalline materials, CMES Comput. Model. Eng. Sci. 96 (2) (2013) 103–115.
[6] A.F. Galvis, P. Sollero, Boundary element analysis of crack problems in polycrystalline materials, Procedia Mater. Sci. 3 (2014) 1928–1933.
[7] A.F. Galvis, P. Sollero, 2D analysis of intergranular dynamic crack propagation in polycrystalline materials a multiscale cohesive zone model and dual reciprocity boundary elements, Comput. Struct. 164 (2016) 1–14.
[8] A.F. Galvis, R.Q. Rodriguez, P. Sollero, Dynamic analysis of three-dimensional polycrystalline materials using the boundary element method, Comput. Struct. 200 (2018) 11–20.
[9] A.F. Galvis, P.A. Santos-Flórez, P. Sollero, M. de Koning, L.C. Wrobel, Multiscale model of the role of grain boundary structures in the dynamic intergranular failure of polycrystal aggregates, Comput. Methods Appl. Mech. Engrg. 362 (2020) 112868.
[10] J.E. Alvarez, C.C. Ramos, A.F. Galvis, P. Sollero, A fully dynamic bridging approach for modeling the intergranular failure mechanisms in 2D polycrystalline materials, Mech. Mater. 159 (2021) 103920.
[11] M. Nygårds, Number of grains necessary to homogenize elastic materials with cubic symmetry, Mech. Mater. 35 (11) (2003) 1049–1057.
[12] M. Kamaya, A procedure for estimating Young's modulus of textured polycrystalline materials, Int. J. Solids Struct. 46 (13) (2009) 2642–2649.
[13] A.F. Galvis, R.Q. Rodriguez, P. Sollero, Analysis of three-dimensional hexagonal and cubic polycrystals using the boundary element method, Mech. Mater. 117 (2018) 58–72.
[14] P. Becley, Electrical Steels for Rotations Machines, Vol. 1, Institution of engineering and technology, 2002.
[15] H. Kwang, AC Motor Control and Electrical Vehicle, Vol. 2, CRC Press, 2019.
[16] A. Deva, P. Pandey, S. Alam, B.K. Sahoo, R. Kumar, S.G. Chowdhury, B. Jha, Processing of low-carbon deep-drawing steel with high plastic anisotropy using two-stage batch annealing cycle, Mater. Eng. Perform. 30 (2021) 1059–9495.
[17] C. Moura, R. Barbosa, T. Oliveira, Effect of grain size on the drawability of the niobium-stabilized ferritic stainless steel ASTM 430, Tecnol. Metal. Mater. Min. 17 (2020) 1–6.
[18] M. Cunha, S. Paolinelli, Non-oriented silicon steel recrystallization texture study, in: Textures of Materials, in: Materials Science Forum, vol. 408, Trans Tech Publications Ltd, 2002, pp. 779–784.
[19] M. Gerlach, M. Zajonc, B. Ponick, Mechanical stress and deformation in the rotors of a high-speed PMSM and IM, Elektrotech. Inf.tech. 138 (96) (2021) 1613–7620.
[20] D. Gerada, A. Mebarki, M. Shanel, N.L. Brown, K.J. Bradley, Design considerations of high-speed induction machines for high-temperature applications, in: 2008 18th International Conference on Electrical Machines, 2008, pp. 1–6.
[21] S. Barrans, M. Al-Ani1, J. Carter, Mechanical design of rotors for permanent magnet high-speed electric motors for turbocharger applications, Electr. Syst. Transp. 7 (2017) 278–286.
[22] Y. Gu, W. Xiaoyuan, G. Peng, L. Xiaoning, Mechanical analysis with thermal effects for high-speed permanent-magnet synchronous machines, IEEE Trans. Ind. Appl. 57 (5) (2021) 4646–4656.
[23] R. Hill, A user-friendly theory of orthotropic plasticity in sheet metals, Int. J. Mech. Sci. 35 (1) (1993) 19–25.
[24] ISO, 6892: Tensile Test - Method of Test at Elevated Temperature, Standard, International Organization for Standardization, 2018.
[25] G. Cortis, F. Nalli, M. Sasso, L. Cortese, E. Mancini, Effects of temperature and strain rate on the ductility of an API X65 grade steel, Appl. Sci. 12 (2022).
[26] M. Kassner, N. Nguyen, G. Henshall, H. McQueen, The effects of temperature and strain rate on extended ductility of aluminum, Mater. Sci. Eng. 132 (1991) 97–105.
[27] ASTM, D7984-16: Standard Test Method for Measurement of Thermal Effusivity of Fabrics Using a Modified Transient Plane Source (MTPS) Instrument, Standard, ASTM, 2016.
[28] C. Zhao, T. Lu, H. Hodson, J. Jackson, The temperature dependence of effective thermal conductivity of open-celled steel alloy foams, Mater. Sci. Eng. A 367 (1) (2004) 123–131.
[29] R. Graves, T. Kollie, McElroy, The thermal conductivity of AISI 304L stainless steel, Int. J. Thermophys. 12 (1991) 409–415.
[30] ASTM, E228-17: Standard Test Method for Linear Thermal Expansion of Solid Materials With a Push-Rod Dilatometer, Standard, American Society for Testing and Materials, 2017.

[31] P. Han, J. Choi, D. Kim, Y. Chun, D. Bang, Thermal analysis of high speed induction motor by using lumped-circuit parameters, Electr. Eng. Technol. 10 (2015) 2040–2045.
[32] Y. Lee, H. Lee, S. Hahn, K. Lee, Temperature analysis of induction motor with distributed heat sources by finite element method, IEEE Trans. Magn. 33 (2) (1997) 1718–1721.
[33] V. Sládek, J. Sládek, Boundary integral equation method in thermoelasticity part I: general analysis, Appl. Math. Model. 7 (4) (1983) 241–253.
[34] V. Sládek, J. Sládek, Boundary integral equation method in thermoelasticity part III: uncoupled thermoelasticity, Appl. Math. Model. 8 (6) (1984) 413–418.
[35] M. Aliabadi, The Boundary Element Method: Applications in Solids and Structures, Vol. 1, Wiley, 2002.
[36] V. Paidar, Elastic properties and model atomic interactions in Fe-Si alloys, Czech. J. Phys. 22 (1972) 938–951.
[37] P. Paufler, The mechanics of crystals and textured polycrystals, Cryst. Res. Technol. 29 (4) (1994) 532.
[38] B.D. Cullity, S.R. Stock, Elements of X-Ray Diffraction, Vol. 3, Pearson, 2014.
[39] H. Hong, W. Lin, H. Lin, H. Chen, Y. Hwu, Y. Chiou, Shape effects of iron nanowires on hyperthermia treatment, J. Nanomater. 2013 (2013) 1687–4110.
[40] A. Schuwartz, M. Kumar, B.L. Adams, D.P. Field, Electron Backscatter Diffraction in Materials Science, second ed., Springer, New York, NY, 2009.
[41] ASTM, E8/E8M: Standard Test Methods for Tension Testing of Metallic Materials, Standard, American Society for Testing and Materials, 2016.
[42] T. Manninen, J. Säynäjäkangas, Mechanical properties of ferritic stainless steels at elevated temperature, in: Fourth International Experts Seminar, Vol. 4, 2012, pp. 1–15.
[43] L. Gardner, A. Insausti, M. Ashraf, Elevated temperature material properties of stainless steel alloys, J. Construct. Steel Res. 66 (5) (2010) 634–647.
[44] W. Voigt, Lehrbuch der Kristallphysik: mit Ausschluss der Kristalloptik, Vieweg Teubner Verlag Wiesbaden, 1966.
[45] A. Reuss, Berechnung der Fliessgrenze von Mischkristallen auf Grund der Plastizitätsbedingung für Einkristalle, J. Appl. Math. Mech. 9 (1929) 49–58.
[46] ASME, B31.1-2018: Code for Pressure Piping, Standard, The American Society of Mechanical Engineers, New York, NY, 2018.
[47] I. Benedetti, M. Aliabadi, Multiscale modeling of polycrystalline materials: A boundary element approach to material degradation and fracture, Comput. Methods Appl. Mech. Engrg. 289 (2015) 429–453.
[48] R. Zhang, R. Dou, Z. Wen, X. Liu, Effects of pressure and temperature on the effective thermal conductivity of oriented silicon steel iron core under atmospheric condition, Int. J. Heat Mass Transfer 125 (2018) 780–787.
[49] D. Nardini, C.A. Brebbia, A new approach to free vibration analysis using boundary elements, Appl. Math. Model. 7 (1983) 157–162.
[50] X.W. Gao, The radial integration method for evaluation of domain integrals with boundary-only discretization, Eng. Anal. Bound. Elem. 26 (2002) 905–916.
[51] J.H. Kane, Boundary Element Analysis in Engineering Continuum Mechanics, Prentice-Hall, New Yersey, 1994.
[52] J. Pyrhonen, T. Jokinen, V. Hrabovcová, Design of Rotating Electrical Machines, John Wiley & Sons, 2014.
[53] P. Fedelinski, M. Aliabadi, D. Rook, The dual boundary element method: inertial stress intensity factors, Trans. Model. Simul. 3 (1993) 267–276.
[54] G. Nigh, M. Olson, Finite element analysis of rotating disks, J. Sound Vib. 77 (1) (1981) 61–78.
[55] E. Albuquerque, Análise de problemas dinâmicos em materiais anisotrópicos usando o método dos elementos de contorno (Ph.D. thesis), Universidade Estadual de Campinas, 2001.
[56] J. Kane, Boundary Element Analysis in Engineering Continuum Mechanics, Vol. 1, Prentice Hall, 1994.